CrossMark

Interaction of Hemispherical Blast Waves with Inhomogeneous Spheres: Probing the Collision of a Supernova Ejecta with a Nearby Companion Star in the Laboratory

Domingo García-Senz[1,2], Pedro Velarde[3,4], Francisco Suzuki-Vidal[5], Chantal Stehlé[6], Manuel Cotelo[3,4],
David Portillo[7,8], Tomasz Plewa[9], and Arthur Pak[10]

[1] Departament de Física, Universitat Politècnica de Catalunya, (EEBE) Av. Eduard Maristany 16, E-08019 Barcelona, Spain; domingo.garcia@upc.edu
[2] Institut d'Estudis Espacials de Catalunya, Gran Capità 2–4, E-08034 Barcelona, Spain
[3] Departamento de Ingeniería Energética, Universidad Politécnica de Madrid, José Gutierrez Abascal 2, E-28006 Madrid, Spain; pedro.velarde@upm.es
[4] Instituto de Fusión Nuclear, Madrid, Spain
[5] Imperial College London, UK
[6] LERMA, Sorbonne University, Observatoire de Paris, PSL, CNRS, Paris, France
[7] IMDEA Materiales, Madrid, Spain
[8] ETSII, UPM, Madrid, Spain
[9] Department of Scientific Computing, Florida State University, Tallahassee, FL 32306, USA
[10] Lawrence Livermore National Laboratory, CA 94550, USA

Abstract

Past laboratory experiments at high energy density have provided insights into the physics of supernovae, supernova remnants, and the destruction of interstellar clouds. In a typical experimental setting, a laser-driven planar blast wave interacts with a compositionally homogeneous spherical or cylindrical target. In this work we propose a new laboratory platform that accounts for curvature of the impacting shock and density stratification of the target. Both characteristics reflect the conditions expected to exist shortly after a supernova explosion in a close binary system. We provide details of a proposed experimental design (laser drive, target configuration, diagnostic system), optimized to capture the key properties of recent ejecta–companion interaction models. Good qualitative agreement found between our experimental models and their astrophysical counterparts highlights the strong potential of the proposed design to probe details of the ejecta–companion interaction for broad classes of objects by means of laboratory experiments at high energy density.

Key words: supernovae: general – hydrodynamics – methods: miscellaneous

1. Introduction

Several important astrophysical problems involve collisions of strong shocks with diffuse or dense, quasi-spherical objects. This class of problems includes, for example, the interaction of a high-velocity supernova ejecta with the circumstellar medium, giving rise to supernova remnants (SNRs), the collision of shock waves with molecular clouds, and the impact of the blast wave born in a supernova explosion with a nearby companion star. These events can be studied by means of astronomical observations, computer simulations, and, more recently, scaled laboratory experiments. The synergy between these three seemingly independent methods is known as *laboratory astrophysics*, and is a relatively recent approach aiming at shedding light on physical processes that are otherwise difficult to observe or simulate. For instance, the main features of SNR dynamics have been successfully reproduced in the laboratory experiments at high energy density (Drake et al. 1998, 2000) and showed good quantitative agreement with observations once appropriate scaling relations were applied (Ryutov et al. 1999). In the context more closely related to the present work, the process of destruction of a spherical interstellar cloud has been quite extensively studied in the laboratory (Kang et al. 2001; Robey et al. 2002; Hansen et al. 2007). These studies highlighted the central role played by hydrodynamic instabilities, mainly the Kelvin–Helmholtz (KH) and Widnall instabilities, in the cloud destruction.

However, obtaining good agreement between laboratory experiments and more complex astrophysical objects may require more sophisticated initial configurations. In particular, problems involving self-gravitating objects may require consideration of density gradients. In the laboratory setting such gradients can be manufactured with the help of layered spherical targets. Also, proximity between the shock source and the target object may demand accounting for curvature effects. For example, the supernova shock and the ejecta display substantial divergence during the shock–envelope interaction in core-collapse supernovae. To study the impact of such effects on the process of mixing in core-collapse supernovae, Drake et al. (2002) and Grosskopf et al. (2013) proposed using diverging laser-driven shocks and multi-layered, hemispherical targets.

In this work we consider a laboratory experiment on the ejecta–companion interaction occurring shortly after a Type Ia supernova (SN Ia) explosion in the single degenerate (SD) scenario (Marietta et al. 2000; Maoz et al. 2014). In the proposed experiment, a laser-driven diverging, hemispherical blast wave collides with a layered, dense spherical target. In general, the present study offers the basis for future experiments relevant to physical scenarios involving self-gravitating objects that display significant density gradients. In particular, spherical two-layer targets ought to capture the basic characteristics of non-degenerate stars with their relatively rarefied envelopes and dense cores.

The design details presented in this paper open up the possibility for future experimental realizations, as has been the case with other proposals with different laboratory-astrophysics applications: for instance, a novel platform to study magnetized accretion disks (Bocchi et al. 2013), and the design of experiments to study photoionization fronts (Drake et al. 2016).

Table 1
Main Features of the Layered Spheres used in the Experiments with the Toy Model

Model	$M_{\rm in}$ (g)	$M_{\rm in}^c$ (g)	E_k (erg)	E_k^c (erg)	$\bar{\rho}_{\rm blast}$ (g cm^{-3})	$\bar{v}_{\rm blast}$ (cm s^{-1})	$v_{\rm cm}^c = \frac{M_{\rm in}^c \, \bar{v}_{\rm blast}}{M_c}$ (cm s^{-1})	$v_{\rm cm}^c$ (hydro) (cm s^{-1})
A	0.435	0.1090	0.064	0.0160	1.660	0.542	0.0138	0.0149
B	0.442	0.1105	0.065	0.0163	0.250	0.542	0.0140	0.0124
C	0.445	0.1112	0.064	0.0160	0.140	0.536	0.0139	0.0128

Note. $M_{\rm in}$, E_k are the mass and kinetic energy of the blast within the solid angle subtended by the outer radius of the spherical envelope and the center of the explosion. $M_{\rm in}^c$, E_k^c are the mass and kinetic energy of the blast within the solid angle subtended by the core. Columns 6 and 7 show the average density and average blast velocity. Column 8 gives the velocity of the center of mass of the core from momentum conservation and column 9 gives the hydrodynamic asymptotic estimate of the core velocity.

One difficulty of the experiments is to produce scaled hemispherical shock waves instead of planar ones. Thus Section 2 is devoted to characterizing the impact of planar and hemispherical shock waves on inhomogeneous spheres. In Section 3 we describe the main features of the SD scenario of SNe Ia and present some large-scale simulations of the collision of the supernova ejecta with a nearby companion star. The insight obtained in the previous sections is used in Section 4 to devise and simulate a laboratory experiment to recreate the SD scenario, including detailed information concerning materials, laser energies as well as the geometrical setting of the experiment. The main results of our work are summarized and discussed in Section 5.

2. Spherical versus Planar Shock Fronts Impacting on Layered Spheres

In this section we want to assess the importance of the adopted geometry of a blast wave hitting dense, layered spheres. In this regard, the interactions between the SNR forward shock with cloud inhomogeneities in the interstellar medium have been the subject of several laboratory-astrophysics studies in the past (Robey et al. 2002; Klein et al. 2003; Hansen et al. 2007). These experiments assumed planar shock fronts colliding with homogeneous spheres, which are typically an order of magnitude denser than the environment. The assumption of planar shock geometry is adequate in this case because the supernova explosion originates in a point-like region located very far from the cloud. However, if the center of the explosion is not too distant from the object, curvature effects have to be taken into account to obtain a realistic depiction of the event. In this regard, it is worth noting the interaction of prompt supernova and nova blast waves with a nearby companion star in compact binary systems or the bubble–bubble and bubble–surface interactions in fluid cavitation problems (Maeda & Colonius 2017).

To gain a general insight into the collision of curved blast waves with stellar laboratory analogs, a simple toy model has been built. This model reduces the star to a two-layer sphere, the *core* and the *envelope*, characterized by their densities, ρ_c, ρ_e and radii R_c, R_e. For illustrative purposes, the density and aspect ratio between core and envelope are taken as $\rho_c/\rho_e \simeq 50$, $R_e/R_c \simeq 2$ (equal core and envelope thickness) to mimic the structure of a Sun-like star (more details on the standard Sun model are presented in Section 4.1). The two-layer sphere is hit by blast waves with different curvatures: (a) spherical "close," with radius $R_{\rm blast} = R_c + R_e$ (model A in Table 1), (b) spherical "far," with $R_{\rm blast} = 3(R_c + R_e)$ (model B), and (c) planar (model C). The impacting mass and kinetic energy had the same values in all three cases, and the equation of state
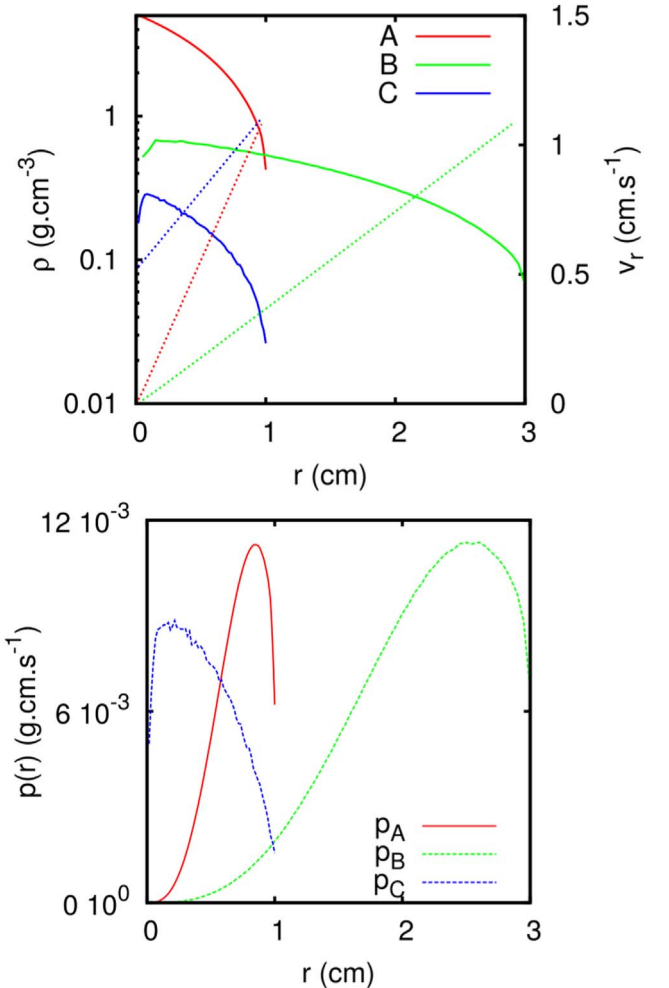

Figure 1. Upper panel: radial profiles of density (solid lines, log scale) and velocity (dotted lines, linear scale) of the blast wave for models A, B, and C in Table 1. Coordinate $r = 0$ is at the origin of the explosion (point-like in models A and B but planar in model C). Lower panel: radial profile of the momentum of the blast wave before the impact.

(EOS) of an ideal gas with $\gamma = 5/3$ was used. Table 1 and Figure 1 summarize the values of the main parameters used in the simulations.

We have carried out several three-dimensional simulations of this toy model with the cutting-edge smoothed-particle hydrodynamics (SPH) hydrocode SPHYNX (Cabezón et al. 2017). SPHYNX's most relevant feature is the use of an integral approach to handle gradients, which is more accurate than the standard SPH procedure. It also displays a better
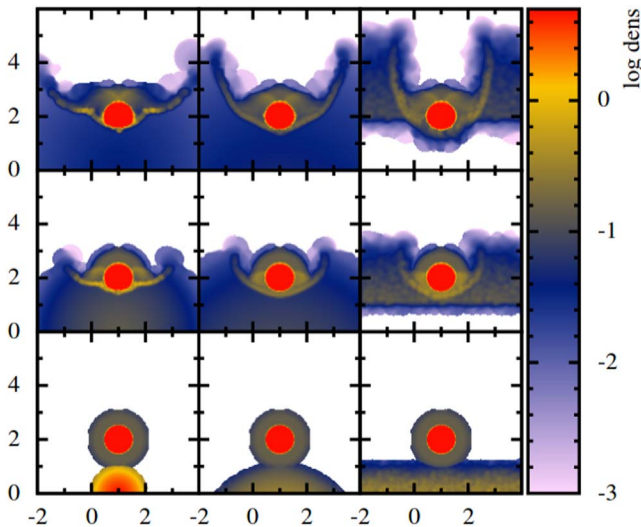
Figure 2. Slice of the density color map depicting the impact of blasts with different geometries (models A, B, C from left to right) on layered spheres at three times, from bottom to top: $t = 0.0$ s, $t = 2.0$ s, and $t = 3.52$ s (the scale of each box is in cm and ρ in g cm^{-3}).

partition of units, which reduces the tensile instability. Both improvements reduce the damping of short wavelengths, thus leading to a better description of instabilities. Two-dimensional slices of the simulations are depicted in Figures 2 and 3. As can be seen, curvature effects have a strong influence in the collision dynamics and thus cannot be disregarded. The planar front leads to a cylindrical-like shape in the post-shock ejecta–envelope region, whereas it becomes conical when the ejecta is spherical (Figure 2). Such an effect is highlighted in Figure 3, where a passive tracer was added to each component of the simulation to better track the geometry of the stripped envelope. These results are reproduced by high-resolution simulations of the laboratory experiment using the code ARWEN, described in Section 4.5. In the experiment, the choice of planar and spherical blast waves leads to very different angular distributions of stripped mass from a two-layer target sphere.

The velocity of the center of mass of the core of the sphere from the toy-model simulation for all three cases is shown in Figure 4. The constant velocity represented by a horizontal line was obtained assuming that the core for case A is totally isolated and momentum is conserved. This agrees with the result of the toy model for case A (red line), with relative differences $\leqslant 13\%$. Also, the maximum relative ratio between models A, B, and C is not large, $\leqslant 20\%$ (see last two columns in Table 1). These differences arise from the particular geometry of the blast wave and the different density profiles in models A, B, and C. The profiles of density and homologous radial velocity at $t = 0$ s are depicted in Figure 1, where the value $r = 0$ cm is the center of the explosion. Although the functional form of the adopted density profiles is the same (i.e., linear with negative slope) the maximum and minimum values among them differ. In particular, the density values are larger in model A, which leads to an enhanced piston effect. Thus, in spite of having a lower component of velocity in the direction of impact, the core of model A gets the largest velocity kick. This is an indication that, besides the geometry, the particular density and velocity profiles of the blast wave are also relevant to obtaining the precise asymptotic velocity of the core. Figure 1 also shows the profile of the momentum along the
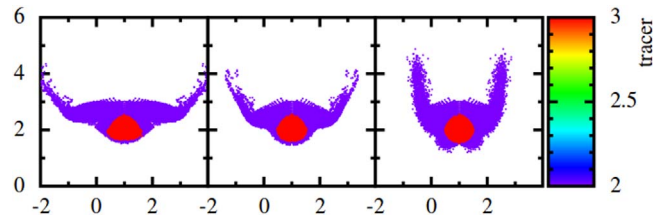

Figure 3. Same as the top row in Figure 2 at $t = 3.52$ s, but directly showing the distribution of the SPH particles belonging to the envelope material (characterized by the magnitude *tracer* $= 2$, in purple) and the core (*tracer* $= 3$, in red).
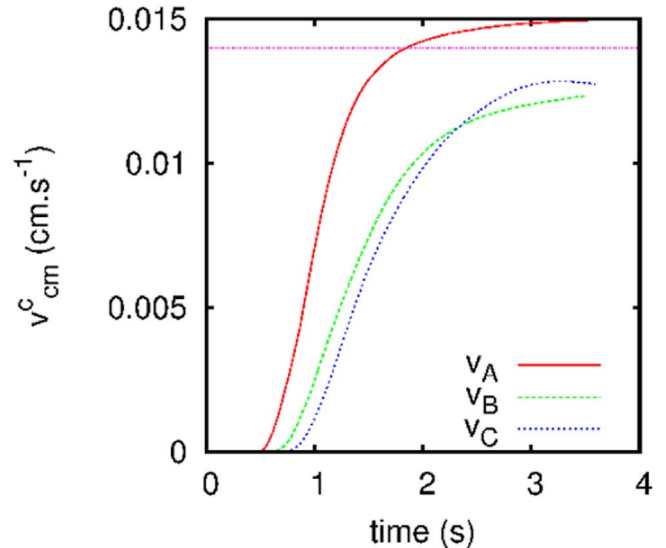

Figure 4. Evolution of the velocity of the center of mass of the core for models A, B, and C. The horizontal line is the core kick velocity obtained using momentum conservation for model A.

blast wave for models A, B, and C. Although the total integrated impacting mass, momentum, and energy are the same in the three cases, their spatial profiles are not.

Finally, it is worth noting that the evolution of models B and C is rather similar. This is due not only to the greater flatness of the blast wave in model B, but also to the smaller differences in the maximum and minimum densities in their radial profiles with respect to model A (see Figure 1, upper panel).

3. Connecting the Impact of Inhomogeneous Spheres with the SD Scenario of SNe Ia

The quest for suitable progenitors of Type Ia supernova explosions is a long-lasting hot topic of stellar astrophysics. Currently, two broad families of progenitors are considered. Both families involve a massive white dwarf (WD, the exploding object) but they differ in the nature of the nearby companion star. In the so-called SD scenario the companion star can be a main-sequence star or a more evolved star (a subgiant or a giant) whereas in the double degenerate (DD) scenario the secondary star is another WD. In the SD scenario the companion star could survive the explosion of the WD (although severely perturbed) while in the DD scenario no remnant is left following the explosion. Therefore, the most straightforward way to distinguish between the two scenarios would be to observationally detect the remnant of the secondary star. In this respect, although the first surveys of field stars around the central region of the Tycho SNR were

promising (Ruiz-Lapuente et al. 2004; Ruiz-Lapuente 2014), recent observations have cast doubt on the existence of such a remnant of the companion star (Xue & Schaefer 2015; Williams et al. 2016; Ruiz-Lapuente et al. 2018).

The identification of the companion star is the most direct, but not a unique way to confirm the SD scenario. During the interaction of the supernova ejecta with the companion, a big portion of the envelope of the companion star is stripped away and the shocked supernova material mixes with the envelope material of the secondary. The temperature in the interacting region rises to $T \simeq 6 \times 10^7$ K, producing an excess of ultraviolet (UV) and soft X-ray transient emission, which has been detected (Cao et al. 2015; Marion et al. 2016). Also, the shielding effect of the companion star produces a low-density region in the otherwise spherical ejecta. Such an ejecta *hole* is a geometric anomaly that may explain the current spectro-polarimetric observations of SNe Ia (Kasen et al. 2004). According to numerical simulations, the center of mass of the secondary receives a radial kick that raises its velocity from zero to $v_r \simeq 100$ km s^{-1} (Marietta et al. 2000; Boehner et al. 2017). In addition, the mixing between the supernova and the secondary material contaminates both objects, thus increasing the hydrogen content of the ejecta as well as the metal content of the surface of the remnant of the companion.

After some hundreds of years, the evolution of the ejecta hole could leave a fingerprint in the structure of the SNR. Specifically, it could affect the geometry of the X-ray emission from the material swept by the reverse shock (García-Senz et al. 2012; Gray et al. 2016). The shadow cast by the companion star has been recently invoked as a possible scenario to explain the asymmetric expansion of the iron ejecta in the Kepler SNR (Kasuga et al. 2018).

The study of the impact of the ejected supernova shell on a nearby companion star is not new (Wheeler et al. 1975), although only since the work by Marietta et al. (2000) has it received sustained interest (Kasen et al. 2004; Pakmor et al. 2008; Kasen 2010; Pan et al. 2010; García-Senz et al. 2012). Very recent works on the subject are those by Gray et al. (2016) and Boehner et al. (2017). The collision of a typical nova ejecta with a main-sequence companion star was recently studied by Figueira et al. (2018), where the fate of the accretion disk surrounding the WD was addressed.

Lacking observations, the study of the interaction between the supernova debris and the companion star relies strongly on hydrodynamic simulations. For the most part, these calculations take advantage of the axisymmetric nature of the collision, and approach the phenomenon with 2D cylindrical coordinates. Calculations in the full three dimensions are typically characterized by lower resolution but are able to better capture the growth of hydrodynamic instabilities (i.e., KH, Ritchmyer–Meshkov, or Widnall instabilities), because the seeds of these instabilities barely have a preferred geometry in nature. A 3D calculation could eventually allow the inclusion of orbital elements into the simulation.

A third route to study the collisional scenario described above is the laboratory-astrophysics approach. A controlled, reproducible laboratory experiment could shed light on many uncertain issues of the SD scenario and be complementary to hydrodynamic simulations. Ultimately, being able to probe the impact between the supernova ejecta and the companion star in the laboratory would aid in the search for the progenitor of Type Ia supernova explosions. In the following section we

Table 2
Main Features of the Binary System at the Moment of Explosion and at the Beginning of the Interaction, Assumed as Starting Time $t = 0$ s (Last Three Columns)

M_{WD} ($M_\odot$)	M_{Comp} ($M_\odot$)	Distance ($R_\odot$)	E_{kin} (10^{51} erg)	$\langle v_{eject} \rangle$ (km s^{-1})	t_{cross} (s)	Ω (sr)
1.36	1.0	2.95	1.28	6700	197	0.36

Note. t_{cross} is the time needed by the ejecta, moving at $\langle v_{eject} \rangle$, to cross the diameter of the secondary star with initial radius 0.95 $R_\odot$ (reduced unit of time). Ω is the solid angle subtended by the Sun-like star with respect to the center of the explosion.

describe the main features of the collision as obtained from numerical simulations of the astrophysical case from its start to around the first hour, once the interaction has ceased.

3.1. Hydrodynamics of the Interaction

In the SD scenario the progenitor WD is accreting mass from a nearby companion star. When the mass of the WD approaches the Chandrasekhar-mass limit, carbon begins to react with itself, causing the explosion of the object (Hillebrandt & Niemeyer 2000). The companion star can be a normal Sun-like star, a main-sequence star with a larger mass, a subgiant, or even a red giant star. An elemental, widely used distance between the WD and the companion star is set by the size of the Roche lobe (RL) at the moment of the explosion. In the RL approach the geometrical features of the initial configuration of the system are, to first order, only a function of the mass of both the WD and the companion star. We note, however, that the RL approach is a limiting case and that, on average, larger separations may be needed to avoid excessive contamination of the supernova spectra with the hydrogen stripped from the companion star (Botyánszki et al. 2018). Table 2 summarizes the values of some relevant magnitudes at the moment of the explosion. For the companion star we have simply chosen the density, temperature, and mean molecular weight of the standard Sun model (Bahcall & Pinsonneault 2004).[11] The density, temperature, radial velocity, and chemical composition of the supernova ejecta were taken from a spherically symmetric hydrodynamical simulation of a Chandrasekhar-mass model of the explosion (model R2 in Bravo et al. 1993, with the homologous velocity rescaled so that the kinetic energy is $E_{kin} = 1.28 \times 10^{51}$ erg). The explosion model was then mapped to a 3D distribution of $N_{eje} = 2.0 \times 10^6$ SPH particles and placed at a distance of 2.95 $R_\odot$ from the center of the Sun-like star, which was in turn described with $N_{star} = 1.5 \times 10^6$ particles.

The evolution of the system was studied in 3D with the hydrocode SPHYNX. A representative snapshot of the interaction is depicted in Figure 5. We can distinguish two shocks: namely the bow shock embracing the companion star (Figure 5 left) and the innermost shock wave traveling through the interior of the Sun-like star (Figure 5 right). The hole created by the companion, with an aperture $\simeq 40°$, is clearly visible. The hypersonic collision heats up both the ejecta and the envelope of the companion to $T \geqslant 10^7$ K (left panel in Figure 6), which is observed as a transient—soft X-ray, UV—

---

[11] An extensive table with detailed values of the standard Sun model used in Bahcall & Pinsonneault (2004) is available at http://www.sns.ias.edu/~jnb/SNdata/solarmodels.html.
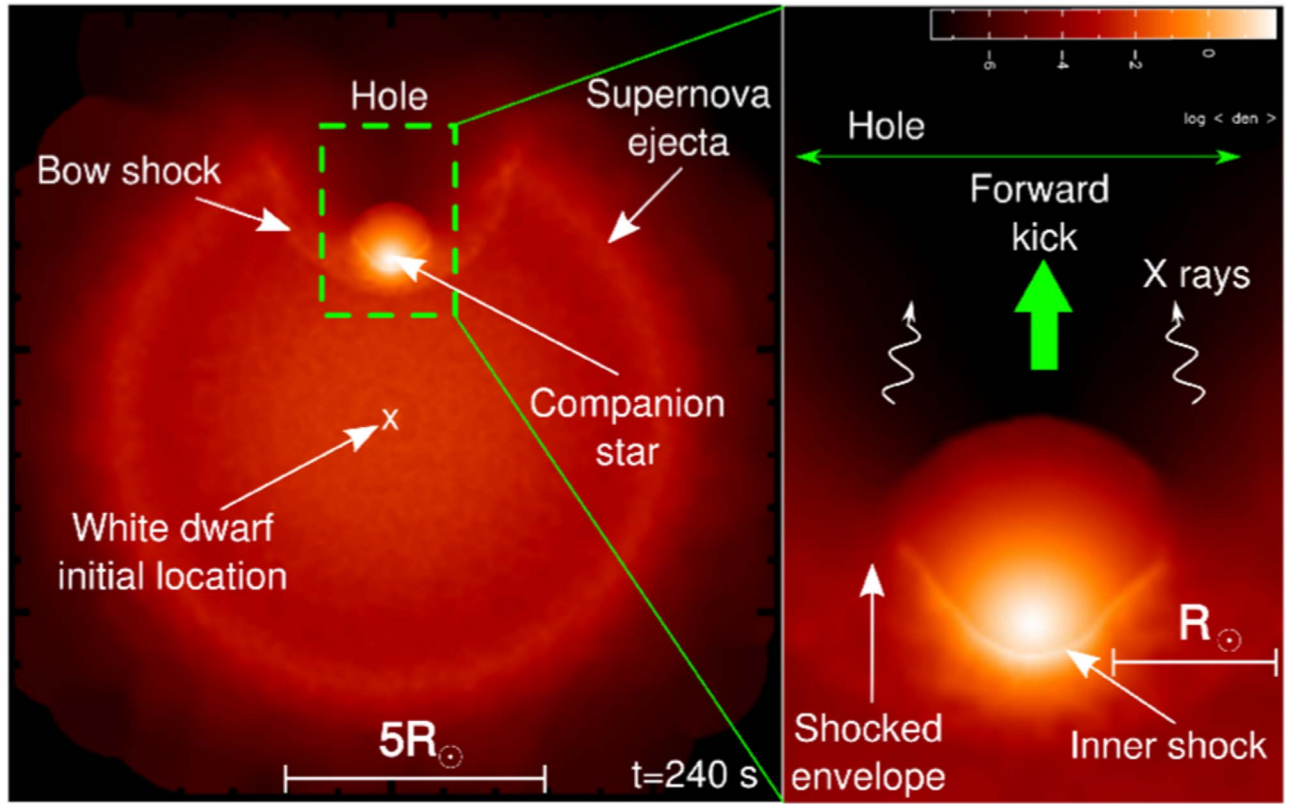
Figure 5. Numerical simulations of the interaction of a supernova with a companion star with the 3D hydrocode SPHYNX. The figures display 2D slices in the collision plane at $t = 240$ s. Both images are density color maps showing $\rho \geqslant 5 \times 10^{-8}$ g cm^{-3} on a logarithmic scale.
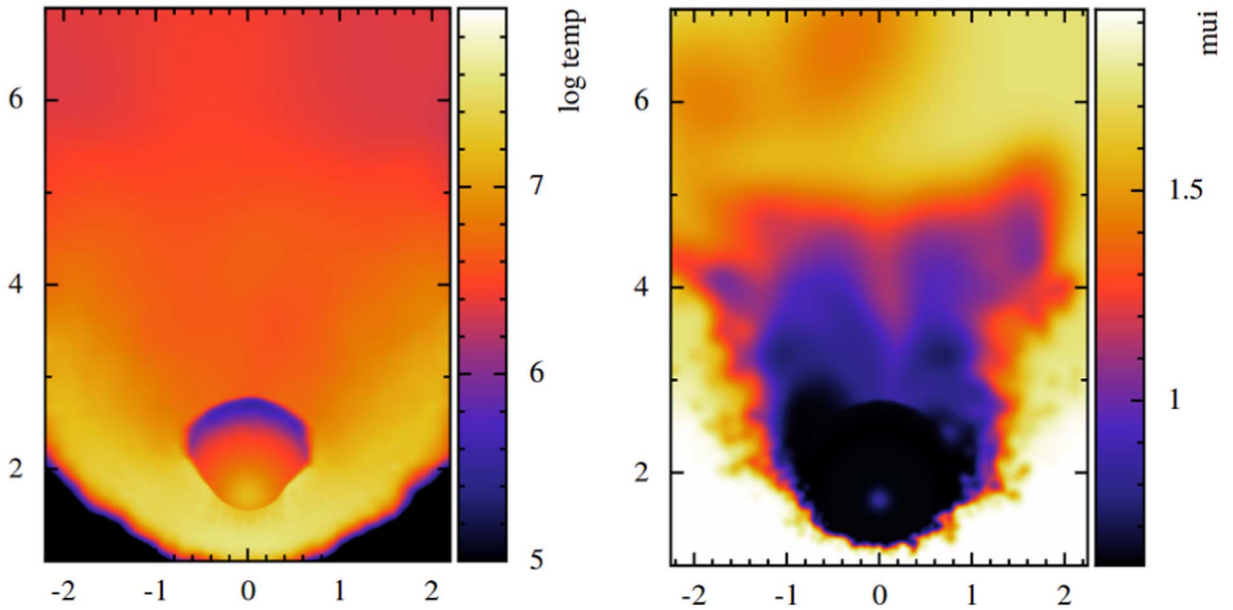

Figure 6. Color maps of temperature (left panel) in kelvin and mean molecular weight (μ_i, right panel) of the interaction region at $t = 226$ s. The stripped material from the companion has $\mu_i < 1$. The corrugation of the contact discontinuity (blue–red contact) between the high-μ_i ejecta material (yellow) and the low-μ_i material of the Sun-like star (blue) is due to the effect of the KH instability. Coordinates are in units of the solar radius.

display lasting from minutes to hours (Kasen 2010; Botyánszki et al. 2018).

A scaled unit of time is obtained by dividing the diameter of the star, $D = 2 R_\odot$, by the average velocity of the homologous ejecta $\langle v_{\text{eject}} \rangle$. Nevertheless, there is no unique way to get $\langle v_{\text{eject}} \rangle$. It can also be estimated from the total mass and kinetic energy

of the ejecta, which results in $\langle v_{\text{eject}} \rangle \simeq 9500$ km s^{-1}. But rather than an energy problem we are facing a momentum problem, so a more compatible estimation with the laboratory experiment is

$$\langle v_{\text{eject}} \rangle \simeq \frac{\langle \rho(r)\, v(r) \rangle}{\langle \rho(r) \rangle} \tag{1}$$
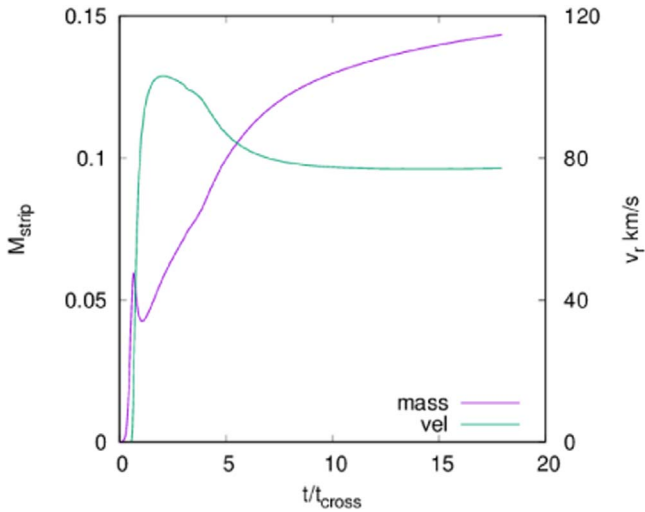
Figure 7. Evolution of the stripped mass (in $M_\odot$) and radial velocity of the center of mass of the remnant of the companion star as functions of the normalized time.

where $\rho(r)$ and $v(r)$ are the radial profiles of density and velocity in the spherically symmetric explosion model. This gives $\langle v_{\rm eject} \rangle = 6700$ km s^{-1} and a crossing time $t_{\rm cross} = D/\langle v_{\rm eject} \rangle = 197$ s (Table 2). The maximum temperature is achieved by the shocked ejecta at the beginning of the collision ($T \simeq 10^8$ K) and decreases with time ($\simeq 5 \times 10^7$ K, $\simeq 3 \times 10^7$ K, and $\simeq 10^7$ K, at $t = 226$ s, $t = 513$ s, and $t = 1043$ s respectively). The shocked region radiates in the soft X-ray and UV bands.

The evolution of the contact discontinuity separating the ejecta from the star material is better addressed in Figure 6 (right), which depicts the distribution of the mean molecular weight μ_i at $t = 226$ s. The mean molecular weight is a good tracer for this purpose because of its different values in the SN ejecta, $\mu_i \geqslant 1.7$, and in the companion star, $0.62 \leqslant \mu_i \leqslant 0.85$. As can be seen, the contact discontinuity (blue–red layer in the lower half of the figure) becomes corrugated and thus prone to develop shear-like instabilities, especially the KH instability (Boehner et al. 2017). The growth of hydrodynamic instabilities around the shear layer might induce mixing of the metal-rich supernova material with the companion star, facilitating the contamination of the remnant of the companion with heavy elements. Nevertheless numerical simulations only show a low or moderate development of hydrodynamic instabilities around the shear region. Thus, the development of the KH and other instabilities does not seem to be very relevant for studying the short-term evolution of the collision. This is, however, a timely open question worth checking in a laboratory experiment. It follows the same line as precedent experiments on the Omega laser, which helped to disentangle the role played by the Widnall instability during the interaction of a shock wave with a solid sphere (Hansen et al. 2007).

The evolution of the stripped mass and the asymptotic velocity of the remnant of the companion are shown in Figure 7. The values obtained with SPHYNX are robust because they are similar to those obtained by other groups (Marietta et al. 2000; Pakmor et al. 2008; Boehner et al. 2017), using very different hydrodynamic codes and semi-analytical estimates (Wheeler et al. 1975).

4. Proposed Experimental Platform

4.1. Building the Laboratory Stellar Analog

We use the results from the astrophysical simulation presented in the previous section to build up a simplified version of the companion star composed of two concentric layers with fixed densities. This will aid in the design of a laboratory stellar analog that can mimic the overall properties of the companion star in the astrophysical case. In order to devise the model, we use the following definitions:

Companion star (Astrophysics $\equiv A$): $\{M_{A2}; R_{A2}; M_{A1}; R_{A1}\}$, where M and R stand for mass and radius, and the subscripts 2 and 1 refer to the companion before and after the collision respectively, i.e., the subscript 1 refers to the innermost region of the companion (the "core"), which survives the collision.

Radial profiles of mass and density for the companion from the standard Sun model before the collision are presented in the left panel of Figure 8, with $M_{A2} = 1\ M_\odot$ and $R_{A2} = 0.95\ R_\odot$.[12] The collision with the supernova ejecta results in mass loss from the outermost radius, leading to the formation of a remnant core and an envelope with an amount of stripped mass $\Delta M_A = M_{A2} - M_{A1}$ and a thickness of $\Delta R_A = R_{A2} - R_{A1}$.

The amount of stripped mass from numerical simulations found in the literature can take any value in the range $0.05\ M_\odot \leqslant \Delta M_A \leqslant 0.3\ M_\odot$, with the precise value depending on the mass and nature of the companion star, the explosion energy, and the geometrical parameters (Marietta et al. 2000; Boehner et al. 2017). For the specific SPHYNX simulation presented in Figure 7, the amount of stripped mass in the companion results in $\Delta M_A = 0.14\ M_\odot$. We use this value on the mass profile from the standard Sun model to infer the radius of the core as $R_{A1} = 0.46\ R_\odot$ (i.e., a thickness of the stripped shell of $\Delta R_A = R_{A2} - R_{A1} = 0.49\ R_\odot$), with a core mass of $M_{A1} = M_{A2} - \Delta M_A = 0.86\ M_\odot$. Notably a collision of this kind would shatter the whole convective zone of the Sun and a half of its radiative zone.

These values allow us to define fixed average mass densities for the core and the envelope for the simplified two-layer companion in the astrophysical case as:

$$\langle \rho_{A1} \rangle = \frac{M_{A1}}{\frac{4}{3}\pi R_{A1}^3} \qquad (2)$$

$$\langle \rho_{\Delta A} \rangle = \frac{\Delta M_A}{\frac{4}{3}\pi (R_{A2}^3 - R_{A1}^3)}. \qquad (3)$$

Radial profiles of average densities for the simplified two-layer companion are presented in the right panel of Figure 8, with the main parameters shown in the first eight columns of Table 3.

4.2. Scaling Relations

We now use the simplified two-layer companion (right panel in Figure 8) to devise a scaled laboratory counterpart. As in the astrophysical case, we define the following parameters:

Laboratory stellar analog (Laboratory $\equiv L$): $\{M_{L1}; R_{L1}; \langle \rho_{L1} \rangle; M_{L2}; R_{L2}; \langle \rho_{\Delta L} \rangle\}$. Similarly $\Delta M_L = M_{L2} - M_{L1}$ and $\Delta R_L = R_{L2} - R_{L1}$.

----

[12] Note that in our numerical three-dimensional approach the radius of the companion is slightly smaller than the standard solar radius.
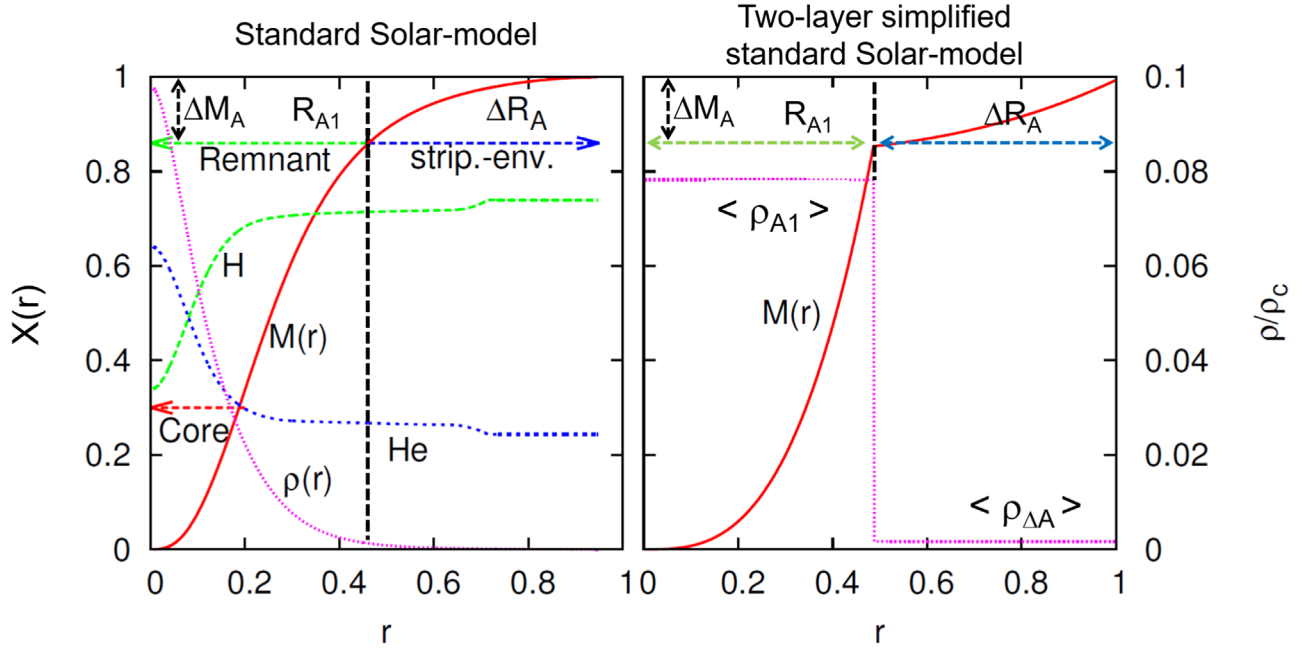
Figure 8. Left panel: profiles of several magnitudes: $\rho(r)$, $M(r)$, $H(r)$, $He(r)$ (generically labeled as $X(r)$) of the standard Sun model. The blue arrow indicates the width ΔR_A of the stripped shell during the collision (inferred using the amount of stripped mass from detailed hydrodynamic simulations with the SPHYNX code), and the green arrow indicates the radius of the remnant companion R_{A1}. Right panel: equivalent simplified two-layer model of the companion star made of two averaged densities (normalized to the central density of the Sun, $\rho_c = 150$ g cm^{-3}) and equivalent radial mass distribution. This information is used to devise the two-layer laboratory target used in the experiment described in the text.

Table 3
Scaling Features of the Companion Star Prior to Impact

M_{A1} ($M_\odot$)	M_{A2} ($M_\odot$)	ΔM_A ($M_\odot$)	R_{A1} ($R_\odot$)	R_{A2} ($R_\odot$)	ΔR_A ($R_\odot$)	$\langle \rho_{A1} \rangle$ (g cm^{-3})	$\langle \rho_{\Delta A} \rangle$ (g cm^{-3})	f	g	h_A	AR_A	v_{A1}^{cm} (km s^{-1})
0.86	1.00	0.14	0.46	0.95	0.48	12.28	0.26	0.16	47.23	7.61	1.04	80.00

Note. The last column shows the asymptotic velocity of the remnant. See Sections 4.1 and 4.2 for the meaning of the different magnitudes.

The physical and geometrical features of the laboratory stellar analog can be obtained from the following equalities:

$$f \equiv \frac{\Delta M_A}{M_{A1}} = \frac{\Delta M_L}{M_{L1}}, \tag{4}$$

$$g \equiv \frac{\langle \rho_{A1} \rangle}{\langle \rho_{\Delta A} \rangle} = \frac{\langle \rho_{L1} \rangle}{\langle \rho_{\Delta L} \rangle}. \tag{5}$$

Combining Equations (4) and (5) we get

$$R_{L2} = (1 + h_A)^{1/3} R_{L1} \tag{6}$$

with

$$h_A \equiv \frac{R_{A2}^3 - R_{A1}^3}{R_{A1}^3}. \tag{7}$$

A characteristic unit of time is set by the crossing time, i.e., the initial diameter of the companion star divided by the average velocity of the supernova ejecta, either in the astrophysical case or in the laboratory,

$$t_{crossA,L} \equiv \frac{2R_{A2,L2}}{\langle v_{A,L} \rangle} \tag{8}$$

where $\langle v_A \rangle = \langle v_{eject} \rangle = 6700$ km s^{-1} for the astrophysical case (Equation (1)).

Similarly, the ratio of the terminal velocity of the center of mass (labeled with the superscript cm) of the spherical remnant

after the impact and the mean velocity of the supernova ejecta can be scaled to the laboratory as

$$\frac{v_{A1}^{cm}}{\langle v_A \rangle} = \frac{v_{L1}^{cm}}{\langle v_L \rangle}. \tag{9}$$

An additional geometrical constraint comes from the ratio of the initial radius of the companion R_{A2} to the distance from the center of the supernova explosion D_A,

$$\frac{R_{A2}}{D_A} = \frac{R_{L2}}{D_L}. \tag{10}$$

The full scaling between the astrophysical case and the laboratory can be obtained from Equations (4)–(10). It is useful, however, to define the aspect ratio between envelope and core in both astrophysics and the laboratory:

$$AR_{A,L} \equiv \frac{R_{A2,L2} - R_{A1,L1}}{R_{A1,L1}}. \tag{11}$$

The main scaling parameters, estimated from the standard Sun model and the hydrodynamic simulations with SPHYNX, are presented in the last five columns of Table 3.

4.3. Scaling Procedure

We propose to study the collision between a supernova ejecta and a nearby companion star in the laboratory by driving
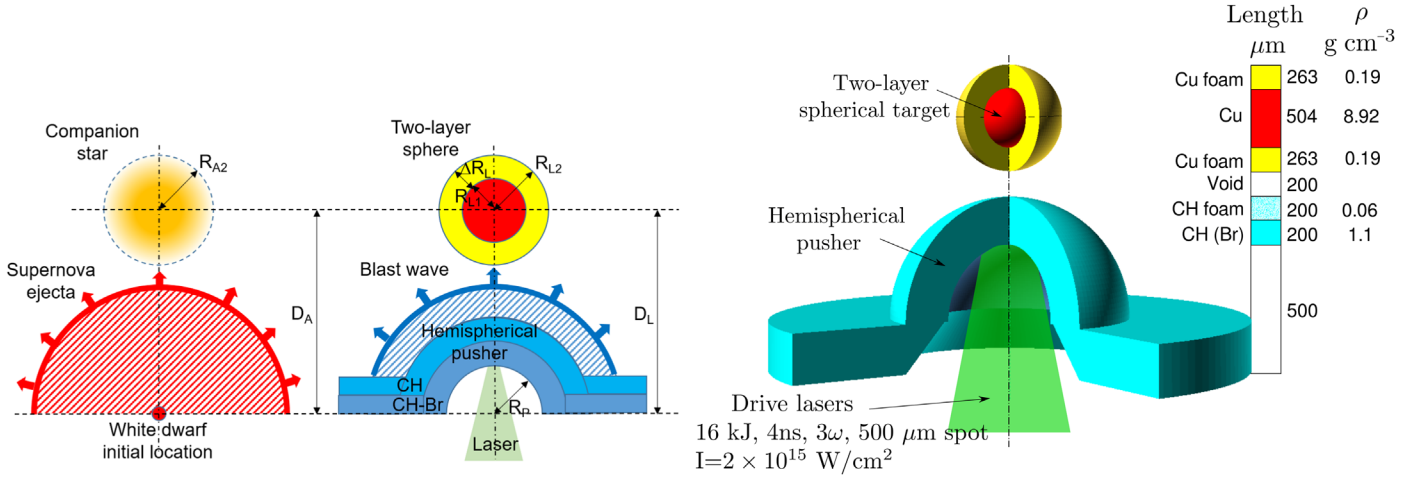
Figure 9. Proposed experimental setup. Left: schematic comparison between the astrophysical case and the laboratory platform. In the laboratory, a high-power laser is focused on the inner surface of a hemispherical pusher, which drives a plasma flow onto a two-layer spherical target. Right: 3D cutaway view of the experimental setup, showing the different materials, lengths, and densities.

Table 4
Main Features of the Laboratory Stellar Analog Prior to Impact after Applying the Scaling Relationships in Table 3

R_{L1} (μm)	R_{L2} (μm)	ΔR_L (μm)	$\langle \rho_{L1} \rangle$ (g cm^{-3})	$\langle \rho_{\Delta L} \rangle$ (g cm^{-3})	AR_L	D_L (μm)	v_{L1}^{cm} (km s^{-1})	v_{CH}^{cm} (km s^{-1})
252	515	263	8.9	0.19	1.04	1615	0.9	55

Note. We assume a solid copper sphere with a radius of $R_{L1} = 252$ μm. See Section 4.3 for the meaning of the different parameters.

a supersonic, spherical blast wave onto a solid, two-layer spherical target. A high-power laser is focused onto a concave, hemispherical cavity (a *pusher*), which produces a curved blast wave. The proposed experiment is depicted schematically in the left panel of Figure 9.

To design the laboratory experiment, the density of the core of the two-layer spherical target ρ_{L1} is chosen as a fixed parameter, while the radius of the spherical core R_{L1} is left as a free parameter. Numerical simulations of the experiment are then performed with the 2D adaptive mesh refinement (AMR) radiative hydrodynamics code ARWEN (Ogando & Velarde 2001), which allows the other parameters of the experiment to be refined.

The iterative procedure works as follows: with the trial value of R_{L1} the total size of the target R_{L2} is estimated with Equations (6) and (7). Equation (10) gives the distance between the pusher and the center of the target, D_L, while Equation (5) gives the density and mass of the envelope of the sphere, $\langle \rho_{\Delta L} \rangle$ and ΔM_L respectively. The terminal velocity of the core of the capsule v_{L1}^{cm} is then compared with the equivalent astrophysical velocity v_{A1}^{cm} (Equation (9)), and the trial value R_{L1} is corrected appropriately. The bisection process driven by R_{L1} is repeated until a satisfactory consistency between the astrophysical and laboratory parameters is achieved.

As an example of a realistic choice of material target, we take a core made of solid copper (density $\rho_{L1} = 8.9$ g cm^{-3}) with a radius $R_{L1} = 252$ μm. The iterative procedure results in the values shown in Table 4.

4.4. Details of the Experimental Platform

The proposed experimental platform in Figure 9 introduces two main differences compared to previous experiments (see e.g., Kang et al. 2001). First, the semi-hemispherical shape of

the ablator introduces curvature to the blast wave in order to reproduce the interaction between the supernova and its nearby companion. Second, the two-layer structure of the spherical target allows us to more realistically mimic the distribution of mass in the companion.

The hemispherical pusher has an inner radius of $R_P = 500$ μm and is made of a layer of a polystyrene doped with bromine CH–Br (200 μm thick, $\rho = 1.1$ g cm^{-3}, directly illuminated by the laser) followed by a second layer of low-density CH foam (200 μm thick, $\rho = 0.06$ g cm^{-3}), which mimics the lower-density envelope of the exploding WD. The Br acts as a shield for the emission of X-rays from the interaction of the laser with the pusher. The two-layer spherical target has an overall diameter of ~1 mm and is made of a solid copper core (diameter $2R_{L1} = 504$ μm, density $\rho_{L1} = 8.9$ g cm^{-3}) with a copper foam outer shell of thickness $\Delta R_L = 263$ μm and density $\rho_{\Delta L} = 0.19$ g cm^{-3}). The distance between the center of the target and the inner surface of the hemispherical pusher is $D_L = 1615$ μm.

As in previous experiments with blast waves impacting on spheres (see for example Kang et al. 2001), the blast wave emerging from the CH foam is separated from the target by a vacuum gap, which is set to 200 μm in our case. Such an empty region is wide enough that the velocity profile of the blast in the pre-impact region becomes homologous (i.e., velocity increases linearly with distance).

As Figure 9 suggests, the process by which the curved blast wave is produced is rather different in the astrophysical and the laboratory scenarios. In the supernova case the blast emerges from a point-like explosion whereas in the laboratory environment it comes after the laser ablation of a hemispherical cavity of finite radius. Nevertheless, despite these different generation mechanisms, the curvature of the blast is nearly the same in both cases, as can be checked by comparing the ratio
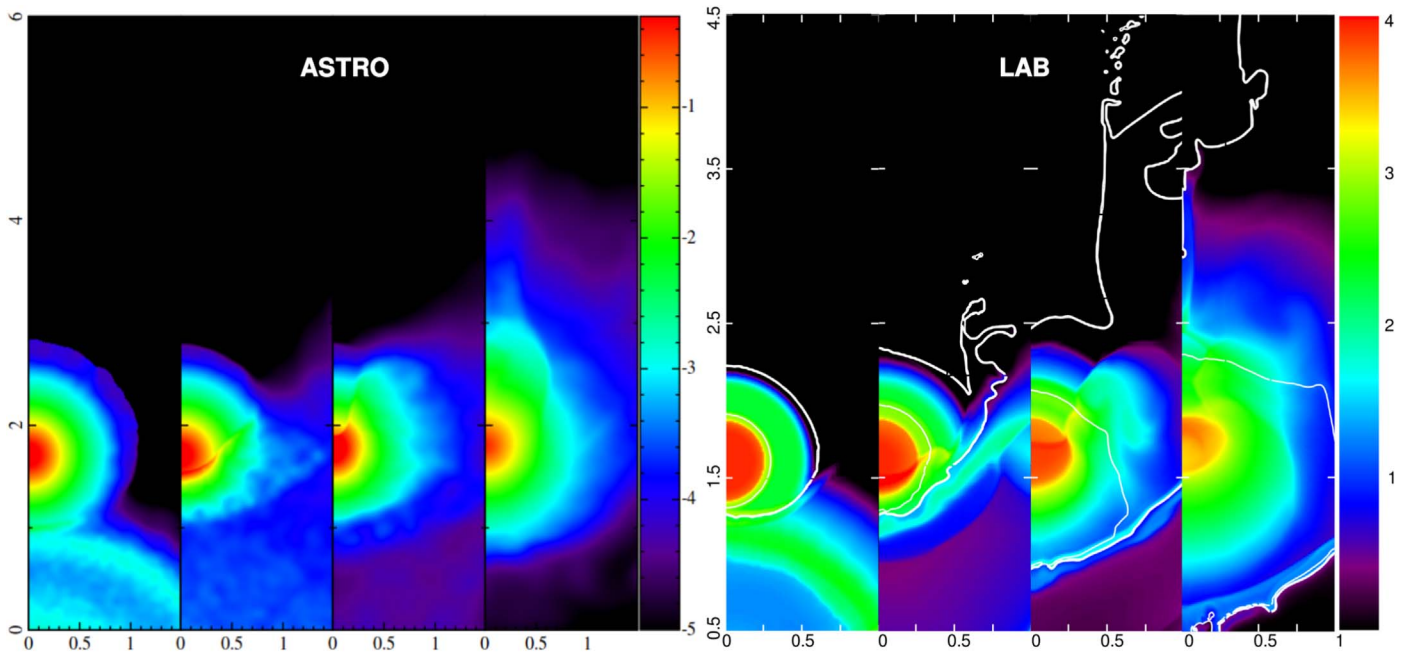
Figure 10. Mass density (log scale) for the laboratory simulation with ARWEN (right, "LAB") and a 2D slice of the 3D astrophysical simulation with SPHYNX (left, "ASTRO"). The frames are at times $t/t_{\mathrm{cross}A,L} = 0.3$, 1.2, 2.6, 5.3, with $t_{\mathrm{cross}L} = 19.4$ ns for LAB and $t_{\mathrm{cross}A} = 197$ s for ASTRO. White lines in the laboratory simulations with ARWEN represent the boundary between materials: Cu (solid), Cu (foam), and CH. Units are solar radius in ASTRO and millimeters in LAB.

between the radius of the target/star and that of the blast-lab./blast-astro. (close to 0.5 in both cases) at the moment of impact. The similarity in blast curvature is also seen in the comparison between the astrophysical and laboratory simulations in the first panel of Figure 10. Additionally, a quantitative estimation shows that the surface radius of the laser-generated blast deviates from spherical symmetry by less than 1% when it hits the target.

4.5. Numerical Simulations of the Experiment

Results from numerical simulations of the scaled experiment with ARWEN are presented in the right panel of Figure 10. To drive the bow shock, a laser with a total energy of 16 kJ, a wavelength of 451 nm (3ω), a pulse duration of 4 ns, and a focal spot with a diameter of 500 μm was used, thus resulting in an intensity of $\sim 2 \times 10^{15}$ W cm^{-2}. These laser parameters are compatible with present high-power laser facilities, for instance one quad of the National Ignition Facility (NIF) laser (Kalantar & Fournier 2016). Resolution is close to 5 μm with a simulation box 7 mm long. The code tracks all the initial material interfaces with negligible diffusion (even with the same thermodynamic properties), allowing the study of doping high-Z elements for experimental observation purposes.

ARWEN is a 2D radiative hydrodynamics simulation code with AMR for both cartesian and cylindrical coordinates. This code couples an unsplit second-order Godunov method for non-diffusive and conservative multi-material hydrodynamics, a flux-limited diffusion package for electron heat conduction, and a multi-group discrete-ordinate (S_n) synthetically accelerated radiation transport module (Garcia-Fernandez et al. 2010). For the AMR structure, it uses the BoxLib[13] package. ARWEN includes the physics required to handle laser ablation with intensities over 10^{10} W cm^{-2} and was designed to perform

calculations of matter in conditions of high energy density, which are common in laser-produced plasmas with laser intensities over 10^{14} W cm^{-2}. It has been applied to different types of systems involving laser-produced plasmas, from inertial confinement fusion (Velarde et al. 2005) to X-ray secondary sources (Oliva et al. 2018) or laboratory astrophysics (Chaulagain et al. 2015). We supply ARWEN with tabular EOSs and opacities to complete the model. The EOSs used in the simulations presented here are based in the quotidian EOS (More et al. 1988) fitted to the available shock-wave experimental data (Cotelo et al. 2011). For the opacities, we used the opacity code BigBART presented by de la Varga et al. (2011, 2013) for LTE conditions. We produce tables of the spectral mass absorption coefficient that are collapsed to the selected number of energy groups for the radiation transport package. BigBART uses the atomic physics code FAC (Gu 2008) to compute self-consistent data such as oscillator strengths or radiative transition energies. The calculations with ARWEN presented in this article were performed with eight groups, six of them with energies below 100 eV. We have run some control cases with 16 groups to check the numerical results. In all the calculations we have used the S_6 approximation for the angular dependence of the intensity, i.e., six directions for sampling an octant in the unit sphere at each spatial point (Castor 2004). In order to check the sensitivity of the results to the order of the angular approximation, some cases were run with S_{10}, i.e., 15 directions per octant.

Figure 10 shows a time sequence of the collision from simulations of the laboratory and the astrophysical cases at the same scaled times $t/t_{\mathrm{cross}A,L} = 0$, 0.3, 1.2, 2.6, and 5.3. For the laboratory case this corresponds to times $t = 0$, 5.8, 23.3, 50.4, and 102.8 ns after the laser pulse hits the pusher, whereas in the astrophysical case this corresponds to $t = 59$, 236, 512, and 1044 s after the supernova explosion. The two simulations show very similar interaction dynamics, e.g., an inner shock is

---

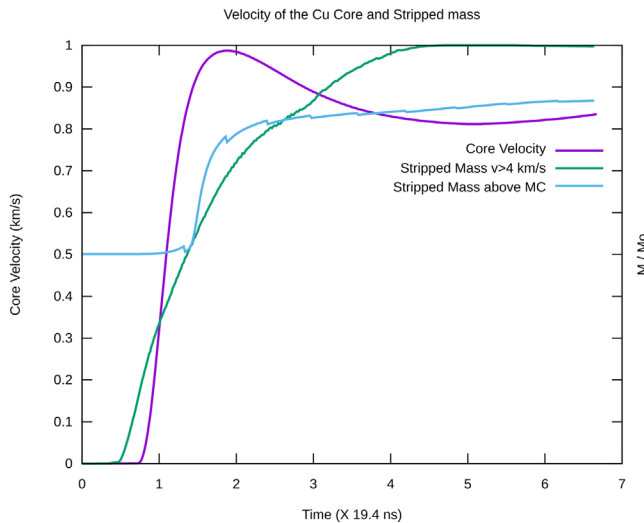[13] Current version AMRex https://amrex-codes.github.io/.

Figure 11. Mean velocity of the copper core of the spherical target and the stripped mass from the envelope as functions of time. Time is scaled with the mean pusher transit time ($\approx$19.4 ns). The stripped mass is normalized with the total envelope mass and is identified as forward ($v_z > 0$) traveling mass above the mass center (MC, blue line). Also plotted is the stripped mass obtained when its velocity becomes larger than 4 km s^{-1} (green line).

driven through the spherical target/companion star (observed at $t/t_{\mathrm{cross}A,L} = 1.2\text{--}2.6$), which precedes the overall motion of the core of the companion as a "kick."

The overall dynamics of the interaction between the ejecta and the companion shows very little difference between the two codes, suggesting that 3D effects (i.e., hydrodynamic instabilities, which eventually could show up in the astrophysical simulation) might not be important in the experiment.

Figure 11 shows profiles of the stripped mass from the target and the average core velocity as a function of the scaled laboratory time $t/t_{\mathrm{cross}L}$ from simulations of the experiments with ARWEN. The evolution of the stripped mass and the size of the Cu core remnant were estimated using two different methods. In the first method we take the criterion that any computational cell of the target is lost when its velocity exceeds a critical velocity, $v_{\mathrm{crit}}^L = 4$ km s^{-1}. Such a critical velocity is close to the escape velocity from the Sun's surface, v_{es}^A, conveniently multiplied by the velocity scaling between astrophysics and laboratory (see Tables 2 and 4),

$$v_{\mathrm{crit}}^L \simeq \frac{v_{\mathrm{CH}}^{\mathrm{cm}}}{\langle v_{\mathrm{eject}} \rangle} v_{\mathrm{es}}^A. \tag{12}$$

The evolution of the stripped mass and core velocity obtained with this criterion is shown by the green line in Figure 11. Our second procedure simply counts as stripped any envelope material with coordinates above the center of mass of the target. This second method leads to the blue line in Figure 11. As can be seen, the precise criterion to decide when the mass element has been stripped mainly affects the rising part of the curves, which is steeper with the second criterion. Nevertheless, both criteria lead to a similar asymptotic behavior. The curves show a similar overall trend to the astrophysical case presented in Figure 7. Furthermore, by taking the ratio between the asymptotic core velocity (AACV) and the average ejecta velocity (AEV) this results in values of AACV/AEV $\approx 1.2 \times 10^{-2}$ and 1.6×10^{-2} for the astrophysical and the laboratory simulations respectively, which fulfills Equation (9).

Figure 12 shows a plot of the angular distribution of stripped mass from the two-layer companion/target. The baseline curve labeled $t = 0$ depicts the mass distribution function of the Cu envelope of the target before the impact (the shell in gray in the sketch) as a function of the axial angle θ ($-90^0 \leqslant \theta \leqslant 90^0$). Figure 12 shows the laboratory and astrophysics $M_{\mathrm{strip}}(\theta)$ distributions at the common time $t/t_{\mathrm{cross}A,L} = 5.3$. The $M_{\mathrm{strip}}(\theta)$ lines for the laboratory and astrophysical simulations lie above the reference line, indicating that much of the stripped material is coming from the lower hemisphere of the target. The consequences of using planar or spherical blasts in the laboratory setting are quite evident from the figure, and support the conclusions from the simple toy model stated in Section 2 above. For curved fronts the agreement between the astrophysical and laboratory simulations is excellent.

5. Discussion and Conclusions

We presented the results of a proposed design for a laboratory experiment at high energy density in which a spherically expanding blast wave collides with a spherical target composed of a dense core surrounded by a low-density shell. The experiment was optimized to match conditions expected to occur during the collision between a supernova ejecta and a non-degenerate, binary companion star in the SD SN Ia formation scenario. The ejecta–companion collision is expected to produce observational signatures that could allow us to constrain binary system parameters and the companion type, and thus advance our understanding of the origins of SNe Ia (see Section 3). Several aspects of this problem could be investigated and verified in the laboratory.

The proposed experiment would enable validation of computer models through comparison of model predictions to experimental measurements in terms of properties of the low-density region (hole) carved by the companion star in the SN ejecta, the velocity kick imparted to the companion by the ejecta, and the prompt X-ray emission produced by the shocked material. The experiment could also provide helpful information about the role of hydrodynamic instabilities in polluting the companion's envelope with the metal-rich SN ejecta material.

The proposed design required addressing some challenging problems. The first issue was the construction of a laboratory analog of the companion star. To this end, we represented a non-degenerate stellar companion as a spherical target composed of a dense central sphere surrounded by a shell made of lower-density material. These two parts represented the companion's core and its envelope, respectively. As discussed in detail in Section 4.1, the physical properties of target components were carefully chosen so that their scaled values closely matched the average density and mass of the corresponding regions of the stellar model. Although the concept of a two-layer sphere may at first appear a crude representation of the real star, it improves upon single-density targets typically used in laboratory experiments (Kang et al. 2001; Klein et al. 2003).

The second important design-related issue was the geometry of the blast wave. The use of planar wave fronts is justified when the distance between the center of the explosion and the target object is much larger than the target's radius. Unfortunately, this condition is not always satisfied in the case of SD SN Ia binary systems. In the extreme case, the orbital distance is only few times the radius of the RL-filling
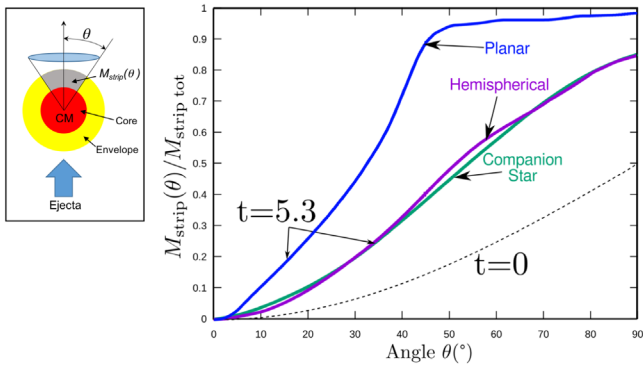
Figure 12. Distribution of stripped mass of the companion star/two-layer target envelope as a function the azimuth measured from its center of mass (CM). The curve labeled "$t = 0$" is the initial mass distribution before the collision. The curves labeled "Companion Star" and "Hemispherical" refer to the astrophysical and experimental simulations respectively. For comparison, the simulation of the experiment using a planar blast wave generated with the same laser conditions (labeled "Planar") is also presented.

Figure 13. Synthetic X-ray radiography from ARWEN simulations of the laboratory stellar analog at scaled times $t/t_{crossL} = 1.39$, 3.25, and 5.21 (left to right). The bottom row shows mass density for each time. The top row shows the transmission coefficient for 18 keV photons (Mo backlighter), with isocontours corresponding to a change in transmission by a factor of 10.
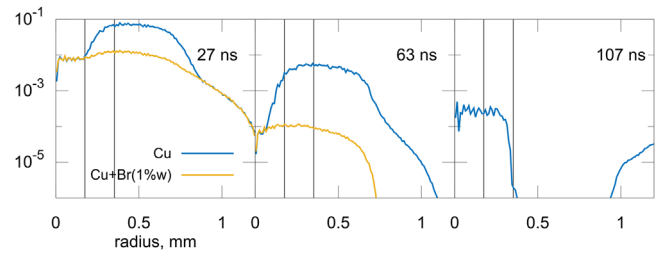
Figure 14. Simulated plasma self-emission as a function of radius from the two-layer spherical target at the same times as Figure 13. The signal (arbitrary units) was averaged over the spectral range 50–150 eV and was produced by a 50 μm pinhole placed 4.385 mm away from the center of the core of the target together with a screen 3 mm away from the pinhole along the pusher–target axis. For each time, the emission from a pure Cu target and that from a Cu envelope doped with Br are compared. The emissivity at 107 ns is negligible for the doped target. The two vertical lines indicate the original radius of the target core and envelope.

companion. In this case, the diverging geometry of ejecta flow must be taken into account in order to correctly describe the angular distribution of the stripped companion's envelope (see Section 2). Our simulation results indicate that curvature effects become negligible if the orbital distance is greater than about five times the companion radius.

Figure 9 shows our experimental design configuration, which accounts for both a composite density structure of the target and the divergence of the blast wave. The blast wave is driven by laser ablation of a hemispherical cavity (a pusher) made of plastic, whereas the target consists of a copper sphere (the core) surrounded by the shell made of copper foam (the envelope). The proposed composite target is made of readily available materials and can be produced using currently available target manufacturing technology.

The simulation results of the experimental system compare very favorably to computer models of the ejecta–companion interaction. The angular distribution of the stripped target envelope material closely matches that of the envelope of the companion star. Also, the evolution of the velocity of the center of mass of the remnant is qualitatively similar in both cases. The asymptotic limiting velocities of the remnants of the stellar analog and companion star agree, after scaling, within 30%. The impact of the blast wave is expected to impart a $\sim$0.9 km s^{-1} velocity *kick* to the core of the companion star. This velocity could potentially be measured via the NIF VISAR diagnostic, which can diagnose velocities as low as 0.5 km s^{-1}. Future work will investigate what modifications to the target geometry would be required, such as a re-entrant cone, to incorporate a VISAR measurement.

Our next goal is to experimentally realize the proposed setup, and to begin to acquire experimental data to compare with our simulation results. The presented model experimental results were obtained using laser parameters currently achievable at large-scale laser facilities, such as the NIF. The proposed experiment requires a modest laser drive energy of 16 kJ delivered by two NIF quads over 4 ns with a top-hat temporal profile. The drive beams are smoothed with phase plates and the spot has a super-Gaussian spatial profile with a 1000 μm FWHM.

The target evolution is diagnosed using an X-ray back-lighting imaging technique. The system uses 18 keV quasi-monochromatic X-rays emitted by a Mo backlighter energized
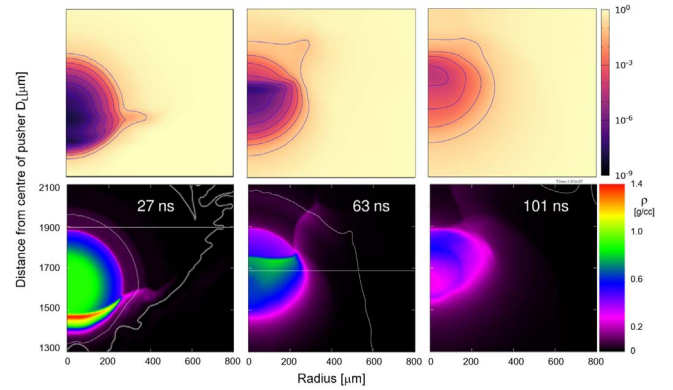
with 36 kJ of energy delivered in 1 ns by four NIF quads. The diagnostic system was optimized with the help of synthetic diagnostics in which hydro simulation results are post-processed using a ray-tracing method. The ray tracer calculates ray paths for a predefined number of rays, with their initial intensities calculated using the local plasma emissivity. Ray trajectories are integrated with their direction changing according to the local value of the plasma refraction index while their intensities are attenuated due to plasma absorption.

The synthetic radiographic images are shown in Figure 13. At early times (left pair of panels in Figure 13), the low-density target envelope is only partially overrun by the shock, which has not reached the dense central core region of the target yet. As time progresses, the incoming flow completely engulfs the target. The shock wave loses strength as it moves into the Cu core, but shocked Cu has a high enough density to remain completely opaque to diagnostic radiation at all times.

Because prompt X-ray and EUV emission is one of the key predicted observational signatures of the ejecta–companion interaction (Kasen 2010; Botyánszki et al. 2018), it is interesting to consider self-emission of the shocked plasma in the corresponding experimental system. Figure 14 shows the radial distribution of the model target emission averaged over the spectral range between 50 and 150 eV, at the same elapsed times as in Figure 13. The emission maps were obtained using a pinhole camera located 6 mm away from the center of the

pusher (i.e., a distance of 4.385 mm between the center of the spherical target and the pinhole), with the imaging plane placed at a distance of 3 mm from the pinhole. The first two panels of Figure 14 show the radial distribution of the emission from the target envelope made of either pure copper or copper doped with 1% bromine. The two target types appear qualitatively and quantitatively different. The emission from the pure copper target is composite in appearance, with the emission from the target envelope dominating at early and intermediate times while the core is the only source of emission at late times. Initially, the emission in the brominated target is rather uniform, with the emission source decreasing in size as time goes on. This suggests that one can obtain more detailed information about shock evolution through the target by using various doping agents, possibly with two or more doped layers.

Furthermore the self-emission and radiography data can also potentially provide additional information about the extent of hydrodynamic mixing between the envelope and core regions and with the pusher material. Imaging the self-emission from multiple lines of sight could allow for the reconstruction of the stripped mass distribution and cone opening angle.

We note that, compared to predictions of astrophysical models (Botyánszki et al. 2018), the target self-emission significantly differs in terms of its spatial distribution and temporal behavior. One possible reason for this difference is the stronger density stratification of stellar envelopes, with the shock energy quickly thermalized in the outermost envelope layers. The prompt model emission is also much harder in the case of the astrophysical system due to a much higher transmitted shock speed and the corresponding temperatures of the shocked envelope material.

ORCID iDs

Domingo García-Senz https://orcid.org/0000-0001-5197-7100
Pedro Velarde https://orcid.org/0000-0001-8615-4905
Francisco Suzuki-Vidal https://orcid.org/0000-0002-7792-4960
Chantal Stehlé https://orcid.org/0000-0003-0484-8773
Manuel Cotelo https://orcid.org/0000-0002-1156-1925
Tomasz Plewa https://orcid.org/0000-0002-1762-2565

References

Bahcall, J. N., & Pinsonneault, M. H. 2004, PhRvL, 92, 121301
Bocchi, M., Ummels, B., Chittenden, J. P., et al. 2013, ApJ, 767, 84
Boehner, P., Plewa, T., & Langer, N. 2017, MNRAS, 465, 2060
Botyánszki, J., Kasen, D., & Plewa, T. 2018, ApJL, 852, L6
Bravo, E., Dominguez, I., Isern, J., et al. 1993, A&A, 269, 187
Cabezón, R. M., García-Senz, D., & Figueira, J. 2017, A&A, 606, A78
Cao, Y., Kulkarni, S. R., Howell, D. A., et al. 2015, Natur, 521, 328
Castor, J. I. 2004, Radiation Hydrodynamics (Cambridge: Cambridge Univ. Press)
Chaulagain, U., Stehlé, C., Larour, J., et al. 2015, HEDP, 17, 106
Cotelo, M., Velarde, P., dela Varga, A. G., & García-Fernández, C. 2011, Ap&SS, 336, 53
de la Varga, A., Velarde, P., Cotelo, M., de Gaufridy, F., & Zeitoun, P. 2011, HEDP, 7, 163
de la Varga, A. G., Velarde, P., de Gaufridy, F., et al. 2013, HEDP, 9, 542
Drake, R. P., Carroll, J. J., III, Estabrook, K., et al. 1998, ApJL, 500, L157
Drake, R. P., Hazak, G., Keiter, P. A., et al. 2016, ApJ, 833, 249
Drake, R. P., Robey, H. F., Hurricane, O. A., et al. 2002, ApJ, 564, 896
Drake, R. P., Smith, T. B., Carroll, J. J., III, et al. 2000, ApJS, 127, 305
Figueira, J., José, J., García-Berro, E., et al. 2018, A&A, 613, A8
Garcia-Fernandez, C., Velarde, P., & Cotelo, M. 2010, ITPS, 38, 2359
García-Senz, D., Badenes, C., & Serichol, N. 2012, ApJ, 745, 75
Gray, W. J., Raskin, C., & Owen, J. M. 2016, ApJ, 833, 62
Grosskopf, M. J., Drake, R. P., Miles, A. R., Plewa, T., & Kuranz, C. C. 2013, HEDP, 9, 439
Gu, M. F. 2008, CaJPh, 86, 675
Hansen, J. F., Robey, H. F., Klein, R. I., & Miles, A. R. 2007, ApJ, 662, 379
Hillebrandt, W., & Niemeyer, J. C. 2000, ARA&A, 38, 191
Kalantar, D., & Fournier, K. 2016, Introduction to NIF, Lawrence Livermore National Laboratory Technical Report, LLNL-PRES-673980
Kang, Y.-G., Nishihara, K., Nishimura, H., et al. 2001, PhRvE, 64, 047402
Kasen, D. 2010, ApJ, 708, 1025
Kasen, D., Nugent, P., Thomas, R. C., & Wang, L. 2004, ApJ, 610, 876
Kasuga, T., Sato, T., Mori, K., Yamaguchi, H., & Bamba, A. 2018, PASJ, 70, 88
Klein, R. I., Budil, K. S., Perry, T. S., & Bach, D. R. 2003, ApJ, 583, 245
Maeda, K., & Colonius, T. 2017, arXiv:1712.00670
Maoz, D., Mannucci, F., & Nelemans, G. 2014, ARA&A, 52, 107
Marietta, E., Burrows, A., & Fryxell, B. 2000, ApJS, 128, 615
Marion, G. H., Brown, P. J., Vinkó, J., et al. 2016, ApJ, 820, 92
More, R. M., Warren, K. H., Young, D. A., & Zimmerman, G. B. 1988, PhFl, 31, 3059
Ogando, F., & Velarde, P. 2001, JQSRT, 71, 541
Oliva, E., Depresseux, A., Cotelo, M., et al. 2018, PhRvE, 97, 023203
Pakmor, R., Röpke, F. K., Weiss, A., & Hillebrandt, W. 2008, A&A, 489, 943
Pan, K.-C., Ricker, P. M., & Taam, R. E. 2010, ApJ, 715, 78
Robey, H. F., Perry, T. S., Klein, R. I., et al. 2002, PhRvL, 89, 085001
Ruiz-Lapuente, P. 2014, NewAR, 62, 15
Ruiz-Lapuente, P., Comeron, F., Méndez, J., et al. 2004, Natur, 431, 1069
Ruiz-Lapuente, P., Damiani, F., Bedin, L., et al. 2018, ApJ, 862, 124
Ryutov, D., Drake, R. P., Kane, J., et al. 1999, ApJ, 518, 821
Velarde, P., Ogando, F., Eliezer, S., et al. 2005, LPB, 23, 43
Wheeler, J. C., Lecar, M., & McKee, C. F. 1975, ApJ, 200, 145
Williams, B. J., Chomiuk, L., Hewitt, J. W., et al. 2016, ApJL, 823, L32
Xue, Z., & Schaefer, B. E. 2015, ApJ, 809, 183